Characterization of cast iron and slag produced by red muds reduction via Arc Transferred Plasma (ATP) reactor under different smelting conditions

Mombelli D.;Mapelli C.;Barella S.;Gruttadauria A.;Ragona M.;Pisu M.;Viola A.

Characterization of cast iron and slag produced by red muds reduction via Arc Transferred Plasma (ATP) reactor under different smelting conditions

D. Mombelli[1,*], C. Mapelli[1], S. Barella[1], A. Gruttadauria[1]
M. Ragona[2], M. Pisu[2]
A. Viola[3]

[1]Politecnico di Milano, Dipartimento di Meccanica, via La Masa 1, 20156 Milano
[2]Centro Ricerche Ecotec, Sesta Strada Ovest, 09040 Uta - Cagliari
[3]Università di Cagliari, Dipartimento di Ingegneria Meccanica, Chimica e dei Materiali, Via Marengo 2, 09123 Cagliari
*davide.mombelli@polimi.it

ABSTRACT
Plasma treatment is a process have demonstrated its feasibility in industrial waste remediation, both for vitrification of toxic wastes into stable slag and recovery of valuable metals from such wastes. In this paper, arc transferred plasma technology was employed for the treatment of red muds, the most concerning waste of Bayer process. Red muds were mixed with different proportion of metallurgical coke (6 and 12 %wt.) and slag conditioners (CaO and SiO_2) and thermally reduced to obtain valuable metals recovery and safe manageably slag. As a function of the mix proportion, reduction of red mud leads to the production of cast iron, accompanied by the formation of a crystalline or glassy slag. Cast iron quality was evaluated trough chemical and microstructural characterization, to identify possible markets where it can be valorised. As well, the different obtained slag where characterized from a chemical, crystallographic, and environmental point of view to identify possible management and valorisation. By an excess of coke, strong iron oxide reduction can be achieved (~95%), with negligible iron loss in the slag (< 2 %wt.). By controlling the basicity (CaO/SIO_2) of the mix, a full developed amorphous slag can be obtained, with a reduced environmental impact and strong inertness against leaching.

1. INTRODUCTION
Treatment of waste has become one of the main concerns of last decades, as traditional waste repositories, such as landfills and dumpsites, are becoming less, less available, and not more sustainable from environmental point of view. In addition, many countries have introduced strict regulations that restrict dumping in landfills, encouraging the implementation of circular economy. For example, in 2015 the "Environmental Protection Law of the PRC" came into force, which strengthened the responsibility of enterprises to prevent and control pollution, and increased legal sanctions against environmental violations [1]. Same laws were adopted in the European Union with the aim to reduce the waste fraction destined to landfill by promoting their recovery in form of secondary raw materials or by-products [2,3]. Use of plasma for treatment of wastes has had a fascination for many years because of its ability to vaporize anything and destroy any chemical bonds. Numerous plasma waste treatment installations have been in operation for many years, offering several advantages in waste treatment. Transferred arc plasma configuration can be efficacy exploited in waste treatment, since the waste material is exposed directly to the plasma arc, which has a peak temperatures in the range 12,000-20,000 K, depending on torch configuration [4]. Transferred arc reactors exist for a very wide range of power levels, ranging from a few hundred watts to tens of megawatts. Plasmas can provide high heat fluxes at high temperatures and high fluxes of reactive species. They can be used for pyrolysis, gasification, stabilization, and vitrification of toxic wastes meanwhile approaching to the recovery of valuable materials within the wastes.
Thermal plasma treatment technology has successfully applied to the treatment of several kind of sludges, like petroleum sludge, tannery sewage sludge, wastewater sludge, storm-water sludge, electroplating sludge, galvanic sludge and a mixture of sewage sludge and fly ash, mainly for stabilization of toxic metals and production of syngas [5–12]. Similarly, thermal plasma treatment technology can be used in the

processing of hazardous metallurgical waste for recovering valuable elements. In example, Mohai and Szépvölgyi [13] converted flue dusts and waste sludges from the hot plating of steel into fine metallic powders by creating a reductive environment in the furnace. Mombelli et al. [14] used an arc transferred plasma reactor to recover the residual iron content within jarosite sludges. The reduction of the jarosite sludges leads to the production of a cast iron, accompanied by the formation of a glassy inert slag that can be used as an alternative to stone material. In the same way, thermal plasma can be exploited for treatment of red muds with the purpose of recovery the iron oxide fraction in form of Fe-based metal. However, only few papers are available on this topic. Jayasankar et al. [15] smelted 47.5 %wt. Fe_2O_3 red muds in batches of 350 g by means of a 35 kW DC arc transferred plasma by varying type and amount of fluxes (limestone, dolomite, quartz and fluorspar), graphite (from 8 to 13 %wt.) and smelting time (13-17 min). Pig iron was successfully produced with an iron recovery of 71 % by the admixing of 11 %wt. of reducing agent, 12 %wt. of dolomite and with a smelting time of 15 min. Rath et al. [16] smelted 37.5 %wt. Fe_2O_3 red muds mixed with lime grit and coke in batches of 500 g by means of a 35 kW DC arc transferred plasma under 10 l/min of argon flux. Statistical designed experiments were carried out to optimize the red muds reduction, that is controlled by reductant and smelting time, and to a lesser extent by basicity. Optimum condition for iron recovery (> 78 %) were found to be 15 %wt. of reductant, basicity of 0.35 and smelting time of 33.46 minutes. However, the formed slag still contained a 7.5 %wt. of unreduced iron oxides. Bhoi et al. [17] reduced 53.6 %wt. Fe_2O_3 red muds in a two-steps process. A magnetic fraction obtained from roasting sintering of red muds-coke mix was used as a feed material for a hydrogen plasma smelting reactor. Steel is then produced with a low amount of slag and water vapor is the only gaseous emission. However, in these papers only thermodynamic assessment of red muds reducibility was taken into account, without any evaluation about the quality of the produced cast iron or its effective marketing, as well without any investigation of the resulting slag properties, toxicity and valorization. In addition, the plasma reactor capacity was limited to hundreds of grams without a real estimation of a full-scale industrial practice [15–17].

In this paper, a pilot-scale arc transferred plasma reactor was employed for the treatment of red muds. In-depth investigation of both cast iron and slag quality was carried out, with the final purpose to identify possible use and markets of such products. The methodology was implemented to solve the critical environmental concerning of red muds lagoon in Portovesme (SU), Italy, where 20 Mm³ of bauxite residues of EurAllumina are stored on an area of 120 ha. The main goal of the plasma treatment is the identification of the best operative conditions to convert the whole amount of available red muds into a marketable Fe-based metallic product and an inert slag fraction, recoverable for civil purposes.

2. EXPERIMENTAL PROCEDURE

2.1 Red Muds characterisation

The chemical composition of red muds was measured through an Energy Dispersive X-ray Fluorecence (ED-XRF) analysis by means of an Ametec Spectro Xepos spectrometer (Kleve, Germany) in He atmosphere (85-90 l/min) on 5 g of powder (size < 100 μm). Crystallographic analysis and phases identification were carried out using a Brucker D8 Advanced Diffractometer (Billerica, Massachusetts, USA) equipped with LynxEye detector (Billerica, Massachusetts, USA). The X-ray analyses (XRD) were performed using Kα 1.5418 Å radiation produced by copper tubes excited by 40 kV and 30 A. Data was collected from 10° to 80° 2θ with a step size of 0.01° 2θ. Peaks identification was performed by exploiting the Crystal Impact Match software (version 3.10.2.173, Bonn, Germany) using the Crystallographic Open Database (COD) (COD-Inorg REV218120 2019.09.10). The morphological characterization was performed by a Zeiss EVO50 Scanning Electron Microscopy (SEM) (Oberkochen, Germany), equipped with an Oxford Inca Energy Dispersive Spectroscopy (EDS) probe (High Wycombe, UK). Detailed results of red muds properties were already published in [18].

2.2. Smelting trials

Red muds sludges were dehydrated and calcined up to 1000 °C in a rotary kiln, to remove imbibition and crystallization water, and to concentrate the iron oxide. The resulting fraction (calcine) was reduced in an arc transferred plasma (ATP) reactor at 1600-1700 °C by the addition of metallurgical coke and fluxes (lime and quartz) in different proportion. Two different trial heats were conducted, with the aim of investigating

two operative conditions largely far from each other. Heat n. 1 were conducted by mixing an excess of coke (12 %wt.) with respect the calcine and using only lime (10-12 %wt.) as flux. The second heat were conducted by mixing the stoichiometric amount of necessary coke (~6 %wt.) and by balancing lime and quartz to obtain a basicity in the range 0.9-1. The reduction reaction led to a separation between a metallic magnetic fraction (indicated as iron) and a non-magnetic fraction (indicated as slag). Experimental conditions and samples labelling are reported in Table 1. The process flowsheet is similar to that followed for the treatment of jarosite [14] and it is protected by an international patent [19].

Table 1. Experimental conditions of the trial heats and samples labelling

Heat	Coke (%wt.)	Lime (%wt.)	Quartz (%wt.)	BI$_2$	Products
1	12	10-12		> 1	iron 1 slag 1
2	6	10-12	4-5	0.9-1	iron 2 slag 2

For these experiments, the calcine reduction treatment was performed in semi-continuous mode (semi-batch) in a 15 litres laboratory furnace, equipped with graphite electrodes and an installed power of 40 kW. Each batch consists of about 10 kg of feeding material (calcine plus additives). The whole study involved the treatment of about 300 kg of red muds. The tap-to-tap time of a single batch was about 30-35 min. The ATP was lined with acidic refractories to prevent any interaction with the slag. The external structure of the reactor is built in stainless steel, with cooling system and temperature control devices. The safety refractory linings (between stainless steel case and reaction chamber) is built in high aluminous refractory.

2.3 Products characterization
The resulting slag were chemically characterized by Wavelength Dispersive X-ray Fluorescence (WD-XRF) and from a microstructural point of view by X-ray Diffraction (XRD), Optical Microscopy (OM) and Scanning Electron Microscopy (SEM).
The environmental impact of the produced slags was determined through a simulated leaching test. A fresh crushed particle (approximately 4 mm in size) for both the slag (slag 1 and slag 2) was leached for 24 hours in demineralized water by varying the L/S ratio from slag 1 to slag 2 (10 and 50 l/kg, respectively) [20]. Slags were characterized by SEM, before and after leaching tests, to detect morphological and chemical alterations, and to make a qualitative comparison on the effects caused by water erosion.

Metallic fraction chemical composition was determined through an Oxford (now Hitachi) Foundry Master Pro Optical Emission Spectrometry (OES) (Chiyoda, Tokyo, Japan), whereas carbon and sulphur content were detected through combustion analysis by the elemental analyser LECO CS230 Series (St. Joseph, Michigan, USA) on 1 g, mixed with iron catalysts to accelerate the combustion and selecting the calibration standards according to the expected theoretical carbon content. Cast iron microstructure was investigated after polishing and etching in Nital 2% for 10 s by means of Optical Microscopy (OM) and SEM. Average Rockwell C hardness was measured according to the ISO 6508 standard, while Vickers micro-hardness was evaluated according to the ISO 6507-1 standard by applying 500 g for 15 s (HV 0.5/15).Transformation temperatures were determined through a Setaram Labsys TG-DSC analysis (Caluire-et-Cuire, France) at 20 °C/min in argon atmosphere (2 Nl/h).

3. RESULTS AND DISCUSSION
3.1. Red muds characterization
     The dried red muds were employed for the reduction trials in form of powder, with a particle size ranging from 2 μm to 5 μm, characterized by 21% wt. of iron oxide and Ti oxides (5% wt.). They also contained alkaline oxide, especially Na_2O (10% wt.) and CaO (5.5 %wt.). Other major constituents were Al_2O_3 and SiO_2 (16%wt. and 10% wt., respectively). From a crystallographic point of view, the raw red mud was mainly formed by gibbsite (γ-Al(OH)$_3$), sodalite ($Na_4Al_3Si_3O_{12}Cl$) and hematite (Fe_2O_3) with traces of boehmite (AlOOH), and calcium and sodium carbonates. Loss of ignition was very high in this kind of waste, reaching approximately the 30% wt., meaning that almost one third of the initial mass is composed by volatile species (i.e., H_2O, CO_2).

Before proceeding with the red mud/reducing agent blend preparation, the red muds were calcined in a laboratory muffle furnace at 1000 °C for 60 min. This preliminary treatment had the purpose to eliminate all hydroxide and carbonate species and some dangerous impurities, to make the material easier to be reduced, i.e. boehmite, gibbsite, sodalite, calcite and thermonatrite. For instance, after calcining, most of the gibbsite and boehmite decomposed into Al_2O_3, while hematite remained unaltered. Al_2O_3 reacted with the decomposition products of sodalite and SiO_2 to form gehlenite. Calcining enabled to concentrate iron oxide, now approximately 30% wt. of the remaining mass. The complete and detailed red mud and its calcine characterization has already been published elsewhere [18]. Chemical composition before and after pretreatment is reported in Table 2.

Table 2. ED-XRF chemical composition of the red muds before and after calcining (% by weight)

	Fe₂O₃	Al₂O₃	Na₂O	SiO₂	CaO	TiO₂	C	SO₃	ZnO	Cl	ZrO₂	MgO	P₂O₅	PbO	Cr₂O₃	V₂O₅	K₂O	MnO	LOI
Fresh RM	20.89	16.30	10.39	9.80	5.54	5.20	4.01	0.30	0.30	0.27	0.24	0.15	0.15	0.14	0.12	0.10	0.08	0.05	29.78
Calcined RM	28.26	21.05	13.44	15.69	7.69	7.26	0.02	0.37	0.46	0.39	0.31	0.22	0.20	0.31	0.17	0.13	0.10	0.07	3.78

3.2. Slag characterization

From a macroscopic point of view, the slag 1 is blue in colour with a crystalline appearance. At high magnification, some cracks in the structure are seen along intergranular planes. The blue colour may depend by the presence of titanates that act as chromatophore elements within the slag microstructure (Figure 1a). By reducing the feed basicity, a glassy slag was obtained (Figure 1b). The surface is dark with lighter veins, which could denote a different chemical composition or a partial devitrification or crystallization. Typical conchoidal fracture surfaces are noted, and the morphology is similar to the slag obtained through the thermal plasma treatment of jarosite sludge [14].
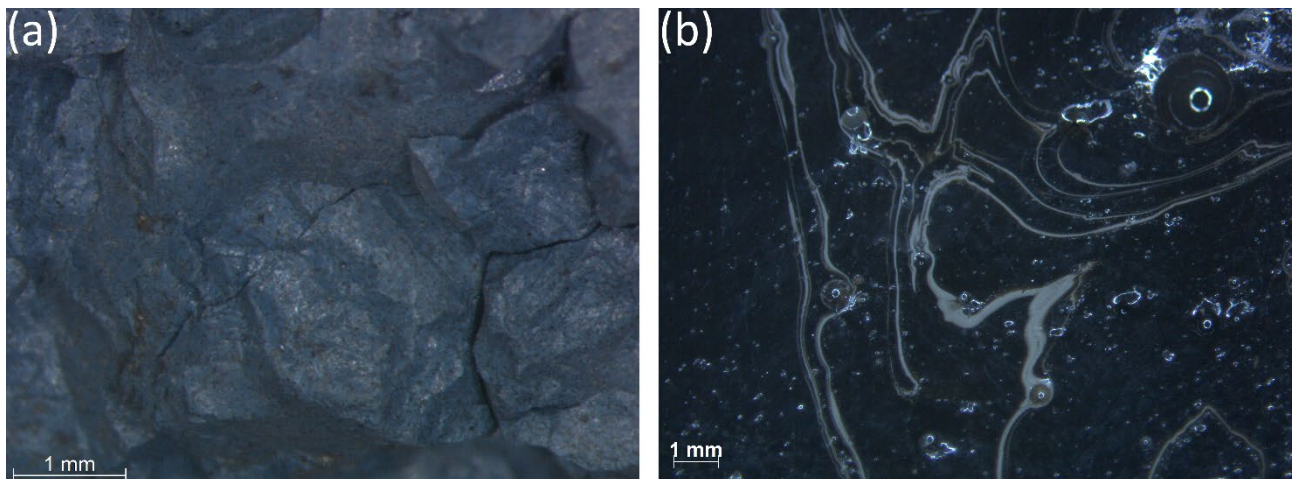

Figure 1. stereo pictures of slag 1 and slag 2 respectively

Slag 1 is essentially a quinary compound of alumina, silica, lime, soda and titania with traces of magnesia, zirconia, potash and sulfur (Table 3). The slag has a binary basicity (BI_2 = CaO/SiO_2) equal to 0.633 and an optical basicity (Λ)[21] equal to 0.666. Despite these values, typical of acidic slag, the slag structure appears totally crystalline, with no evident amorphous fractions. The limited silica content does not allow to consider this slag as a magmatic rock, and consequently to classify it by the Total Alkali Silica Diagram [22–24]. However, using the ternary diagram proposed by De La Roche [25] it is possible to forecast the mineral content of the slag. This slag can be considered as an effusive rock, therefore an ionic solution of oxides that undergoes rapid cooling at atmospheric pressure. On the Ri-Rs-Rm ternary diagram, the slag is positioned in the under-saturated silica zone (Figure 2a), outside the projection of the tetrahedron of Yoder and Tilley in the plane [26]. Using the lever rule in the hercynite-nepheline-anorthite (Hc-Ne-An) sub-region, it is possible to estimate the mineralogical composition of the slag: anorthite (An): 30%; nepheline (Ne): 45% and spinel (Hc): 25%. This approximation is confirmed by determining the standardized mineralogical composition by applying the CIPW norm [27–29]. The standardized mineralogical composition represents an ideal composition, which may not be reflected in the true nature of the rock,

since it is based on several simplifying hypotheses [27–29], i.e. the impossibility of forming hydrate compounds and the assumption that some phases are incompatible with each other. The standardized composition for slag 1 is anorthite (An): 50%, nepheline (Ne): 35% and perovskite (Per): 15%. The differences between the two formulations are obviously linked to the different way of combining the oxides together in forming mineralogical phases of different nature. Calculations according to the CIPW norm also allow to estimate liquidus temperature and density, which for slag 1 are equal to 1604 °C and 2.83 g/cm^3, respectively.

Table 3. WD-XRF chemical composition of slag 1 and slag 2 (% by weight)

Slag	Al$_2$O$_3$	BaO	CaO	C	Fe$_2$O$_3$	K$_2$O	MgO	Na$_2$O	SO$_3$	SiO$_2$	TiO$_2$	V$_2$O$_5$	ZrO$_2$
1	33.64	0.08	18.04	-	1.80	0.12	0.50	8.60	0.10	28.51	8.35	0.12	0.34
2	25.58	0.77	14.75	0.67	3.21	0.25	0.60	8.82	0.48	39.04	5.42	0.11	0.30

Slag 2 is still a quinary compound of silica, alumina, lime, soda and titania (Table 3). A higher residual amount of iron oxide is observed compared to the previous sample whereas there is a higher concentration of SiO$_2$ and consequently a dilution of the other constituents. This is due to the different preparation of the charge bed in the ATP oven (addition of quartz to reduce basicity and less coke). The higher amount of unreduced iron oxide can be due to an increase of slag viscosity, that is not favorable to maximize the separation from metal to slag. This was also confirmed by Jayasankar et al. [15]. In addition, the use of stoichiometric amount of coke does not help in this sense, because the reductive conditions are less severe than in heat 1 and part of the coke is consumed for the reduction of the other reducible oxides (Cr$_2$O$_3$, Na$_2$O, V$_2$O$_5$, ZnO, etc.) [30]. Therefore, this slag has a binary basicity equal to 0.378 and an optical basicity equal to 0.634. These values are typical of acidic slag and conform to the glassy appearance of this sample. The higher silica content makes it possible to classify the slag as a magmatic rock [22–24]. For the TAS diagram [24] (Figure 2b), the sample under examination falls into the family of foidite, i.e. an alkaline rock without feldspar, similar to nephelinite. However, by analogy with the sample 1, it is also interesting to classify the slag using the ternary diagram proposed by De La Roche [25]. The slag is positioned again in the under-saturated silica area (Figure 2a). The portion of the diagram that characterizes this slag (Ne-An-Hc sub-region) is in accordance with the definition of the TAS diagram. Being not crystalline, the determination of the probable phases does not make sense. However, by determining the standardized mineralogical composition (CIPW norm), the probable formation of about 10% of perovskite (Per) is reasonable, due to the presence of a moderate content of titanium oxide, which acts as a glass breaker. The liquidus temperature and density, still estimated through the CIPW norm, are respectively 1400 °C and 2.80 g/cm^3. Compared to the previous sample, the estimated liquidus temperature is reduced of approximately 200 °C, and this aspect can reflect into an energy optimization of the thermal process conducted in the plasma oven.
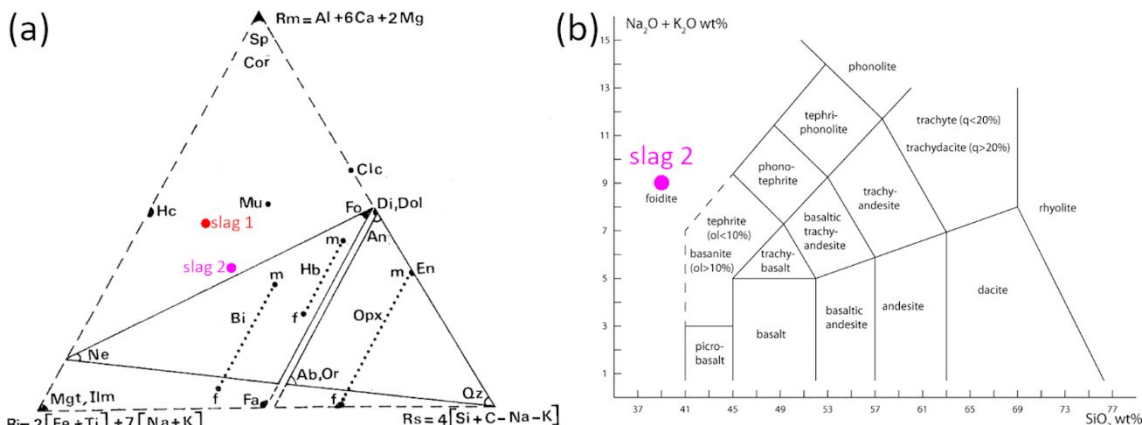

Figure 2. Slag chemical composition indication on Ri-Rs-Rm diagram (a) and TAS diagram (b)

XRD analysis (Figure 3) confirms the overwhelming crystallinity of slag 1. Identified phases are nepheline ((Na,K)AlSiO$_4$), gehlenite (Ca$_2$Al(AlSi)O$_7$) and perovskite (CaTiO$_3$). These compounds are the same predicted

5

by CIPW calculation and their amount calculated through Rietveld method is in agreement (Ne: 79 %wt., G: 11 %wt., Per: 10 %wt.).

Slag 2 was instead confirmed to be amorphous, with a residual < 10% of crystallinity. The peaks at 9 and 44.5 °2θ, are related to quartz and iron, respectively.
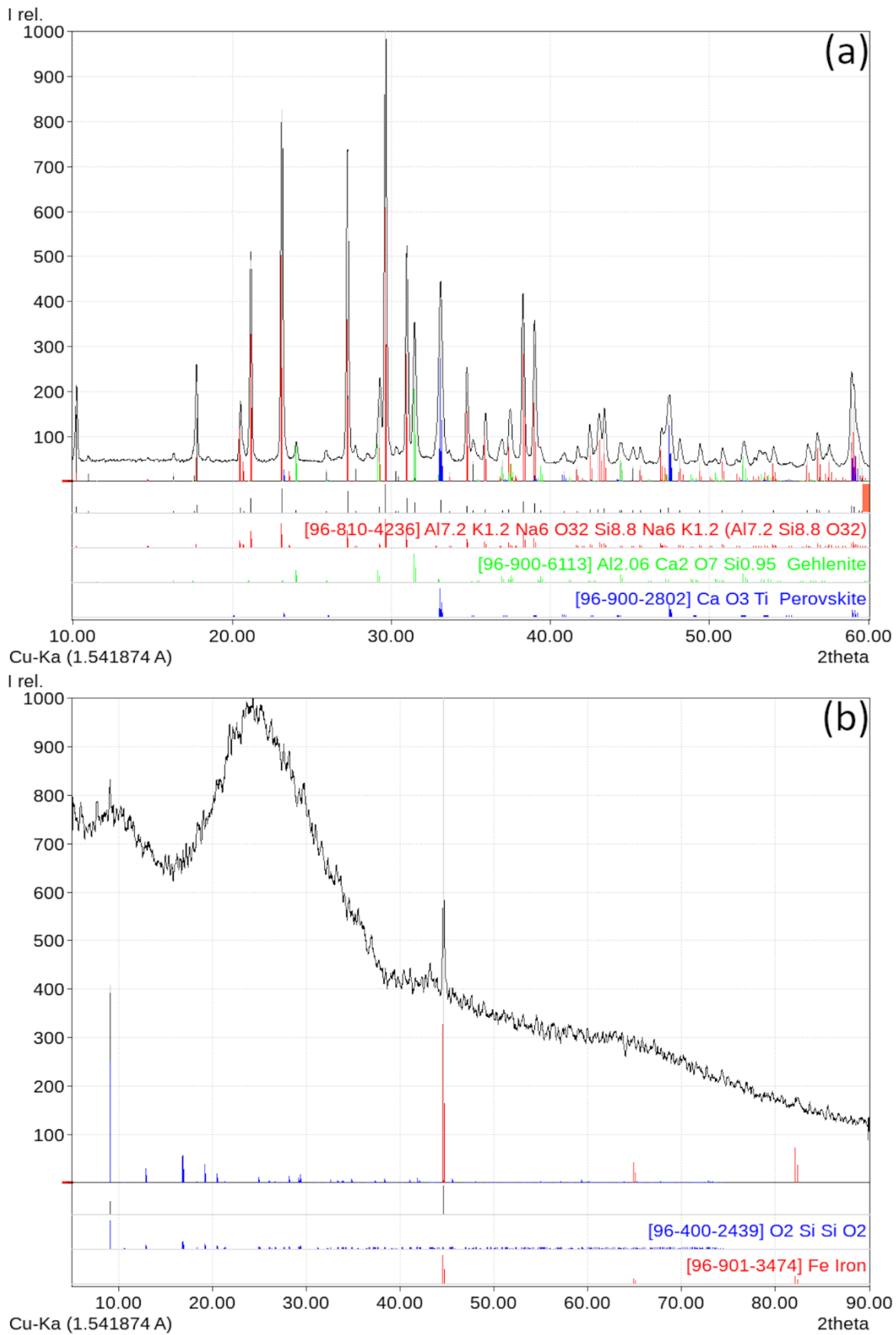
Figure 3. XRD pattern of slag 1 (a) and slag 2 (b)

Optical microscope (OM) observation in polarized light (Figure 4) shows that the slag 1 is composed of a homogeneous crystalline matrix where elongated crystals of different chemical composition were

nucleated (Figure 4a). There are also small metal droplets that have been trapped inside the slag, which in some areas are concentrated in larger volumes.

Slag 2 is composed of a homogeneous glass matrix, where partially developed dendritic crystals were nucleated. There are also small metallic droplets, as well as in slag 1. The analysis of the polished surface allowed to better understand the morphology and the appearance of the light veins highlighted by the stereoscopic observation. These areas seem to consist of a multitude of small crystalline nuclei formed in the liquid glass which, have not had time to grow probably due to the rapid cooling of the mass. The observation in optical microscopy also confirms that the metal inclusion found in the slag is a residual fraction of cast iron, as evidenced by the graphite lamellae present in it (Figure 4b).
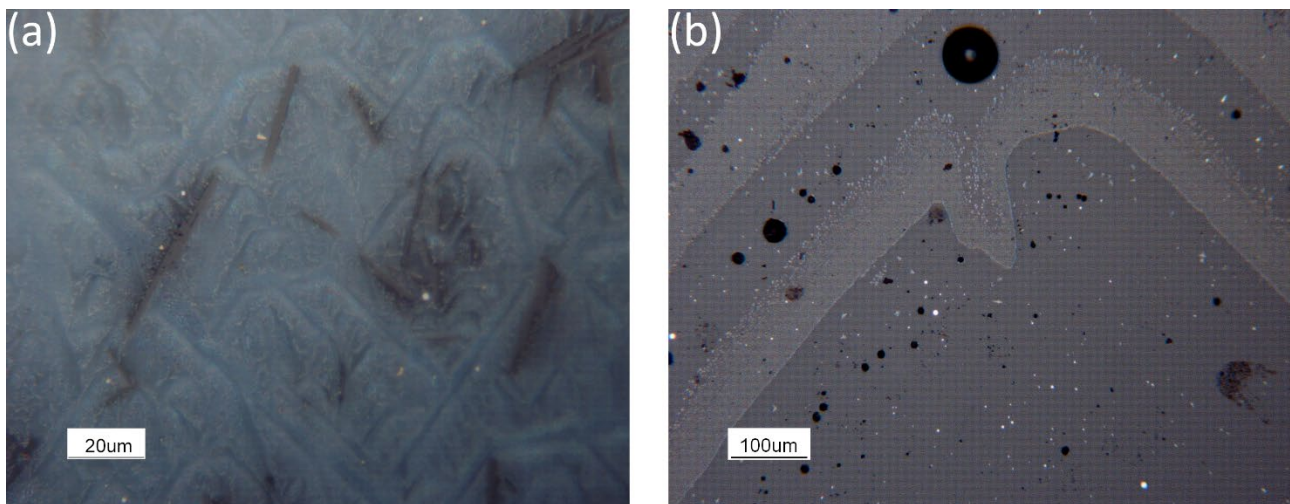

Figure 4: optical microscopy analysis of slag 1 (a) and slag 2 (b)

SEM analysis allowed to clearly identify the different chemical composition of the nucleated crystals within the slag matrix (Figure 5). Slag 1 is mainly composed of sodium, aluminum, silicon, calcium and titanium oxides. Its matrix (A) has a chemical composition lower in Ca with respect the general one (Table 4). Exploiting the quaternary diagram Al_2O_3-CaO-Na_2O-SiO_2 (Figure 6a) and its sub-region $Al_2O_3.SiO_2$-$CaO.SiO_2$-$Na_2O.SiO_2$ (Figure 6b) it can be deduced that it consists of a solid solution of anorthite ($CaO.Al_2O_3.2SiO_2$), albite ($Na_2O.Al_2O_3.6SiO_2$) and nepheline ($Na_2O.Al_2O_3.2SiO_2$), in accordance with what is estimated according to the CIPW standard. Given the atomic% ratios between the different elements, a $Na_2O.CaO.Al_2O_3.2SiO_2$ type structure could be assumed. This compound has the same crystal structure of nepheline, since XRD only detected nepheline as a major compound. The coarse crystals (B) have a typical chemical composition of gehlenite ($2CaO.SiO_2.Al_2O_3$), while the finer crystals (C) are rich in Al, Ca and Ti and could be perovskite-like structures ($CaTiO_3$) enriched in alumina (Figure 5a). More likely, Al and Si derive from the matrix, given the small size of the crystals. These results are consistent with XRD analysis. The metal droplets trapped in the slag are mainly composed of iron (D). It is worthy to mention that the reduction conditions have also led to a partial reduction of titanium oxide, as identified by the areas marked with E at the edges of the iron drops (Figure 5b).

The small droplets identified by OM in slag 2, are both droplets of cast iron not separated from the slag (A and C in Figure 5c) and iron sulphides (zone B and D in Figure 5c). The lighter veins are a multitude of small perovskite crystals nucleated from the liquid. In fact, the local chemical composition inside the striations is rich in Ca and Ti, with respect to the slag matrix (F, G, H in Figure 5d). By the position of matrix chemical composition on the quaternary diagram Al_2O_3-CaO-Na_2O-SiO_2 (Figure 6a) and its sub-region $Al_2O_3.SiO_2$-$CaO.SiO_2$-$Na_2O.SiO_2$ (Figure 6b) it is possible determine its liquidus temperature, which is equal to about 1400 °C, in accordance with what calculated by the CIPW norm.
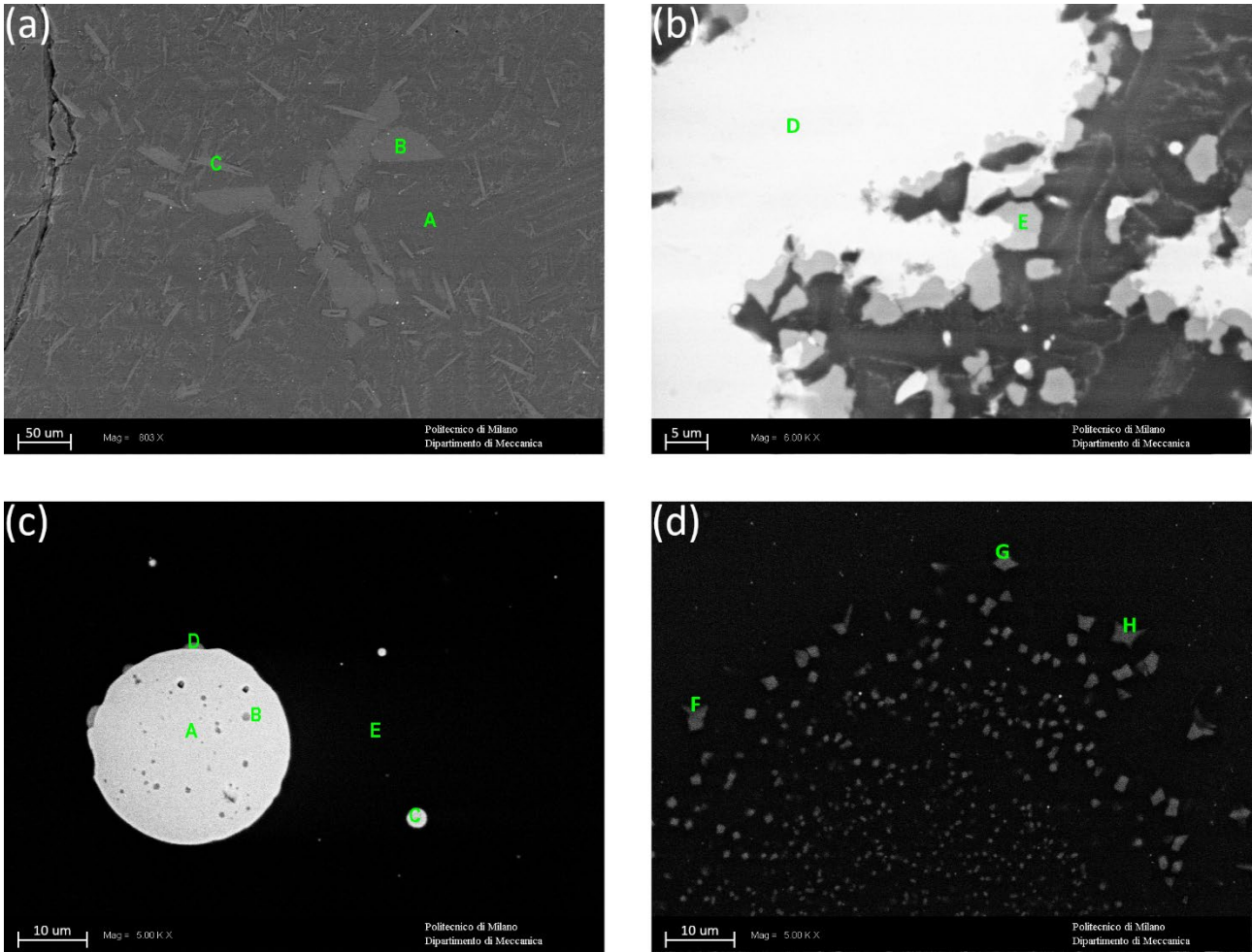
Figure 5. SEM pictures of the slag 1 (a-b) and slag 2 (b-c)

Table 4. General and local slag chemical composition by SEM-EDS analysis (% by weight)

		Na	Mg	Al	Si	S	Ca	Ti	V	Cr	Fe
Slag 1	**General chemical composition**	8.46		30.82	26.98		24.18	9.57			
	Figure 6(a)-**A**	9.87		31.13	28.80		20.96	9.24			
	Figure 6(a)-**B**	1.25		27.39	23.64		47.71				
	Figure 6(a)-**C**		3.74	32.44	8.20		17.70	37.92			
	Figure 6(b)-**D**				3.28					2.11	94.61
	Figure 6(b)-**E**						0.59	84.46	12.81		2.15
Slag 2	**General chemical composition**	7.91		20.18	34.67		28.14	7.70			1.39
	Figure 6(c)-**A**										100.00
	Figure 6(c)-**B**					9.42				0.40	90.18
	Figure 6(c)-**C**				0.73		0.79				98.48
	Figure 6(c)-**D**	2.46		3.98	4.98	22.85	3.43	0.71		1.82	59.78
	Figure 6(c)-**E**	8.45		19.98	34.75		28.42	7.09			1.32
	Figure 6(d)-**F**	3.95		9.31	13.69		36.16	36.89			
	Figure 6(d)-**G**	3.30		6.99	10.34		38.38	40.98			
	Figure 6(d)-**H**	7.61		17.53	29.45		30.66	14.74			
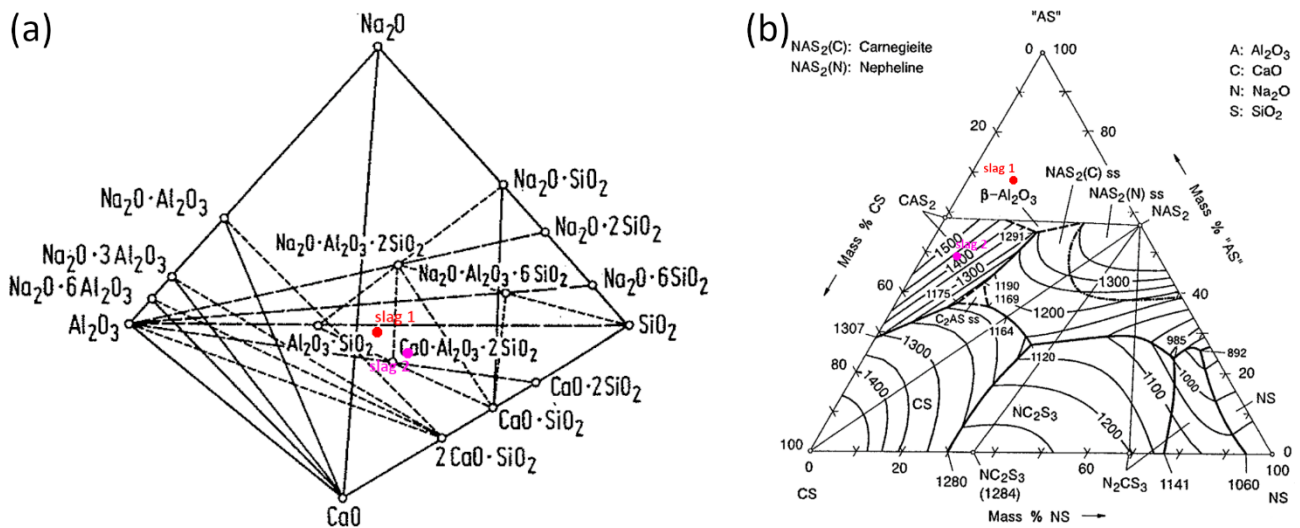
Figure 6. slag matrix chemical composition on Al_2O_3-CaO-Na_2O-SiO_2 quaternary diagram (a) and $Al_2O_3.SiO_2$-$CaO.SiO_2$-$Na_2O.SiO_2$ (AS-CS-NS) ternary diagram (b). Red point = slag 1, pink point = slag 2 [8].

Exploiting such slags for further applications depend upon compliance with the leaching limits of toxic elements as laid down in several decrees. In slag 1, the detection of potentially harmful elements (Cr, V, Ba, Mo, Sb) for humans and environment was negative. The crystalline structure of the slag, being mainly composed of stable phases (anorthite-nepheline, perovskite, gehlenite) should not have problems with leaching of such toxic metals [31]. To prove this, a simulated leaching test by immersing a freshly crushed slag particle in demineralized water for 24 hours was carried out.

The results of simulated leaching test confirm the slag stability, since nor appreciable morphological variations of the slag surface neither chemical composition difference were identified, before and after the immersion (Figure 7a and b). What is most noticeable is a slight oxidation of the cast iron droplets trapped in the slag (white dots). As expected, the only elements that show a slight drop ($\approx$ 1% wt.) were sodium and calcium (Table 5), i.e. those alkaline cations with the highest mobility, and therefore the greater aptitude to move into solution. In particular, their dissolution could lead to obtaining an alkaline leachate, which must then comply with the threshold imposed by the regulation about the simplified recovery procedures for industrial by-products (pH <12) [32]. Based on this results, slag 1 can be considered inert and therefore disposed of in landfills without further treatment. For its recovery as an aggregate for unbound applications (ballast railway, aggregates for foundations, etc.) its compliance with the threshold concentrations imposed by regulation [32] must be verified.

Similarly, also in slag 2 nor noticeable change in morphology (Figure 7c and d) neither in chemical composition (Table 5) can be observed, despite the L/S ratio adopted being five times higher than the previous one. This clearly indicates that obtaining a glassy slag guarantees better safety in terms of environmental sustainability, as it results in better product stability, minimizing the risk of toxic metals leaching. For slag 2, the only element has undergone a dilution, even if less than before, was sodium. Thus, slag 2 can be considered inert and therefore disposed in landfills without any further treatment. Its recovery as aggregate could be easier than slag 1, since its behaviour in leaching test is expected to be similar to the slag obtained by the treatment of jarosite in the same arc transferred plasma reactor [14].
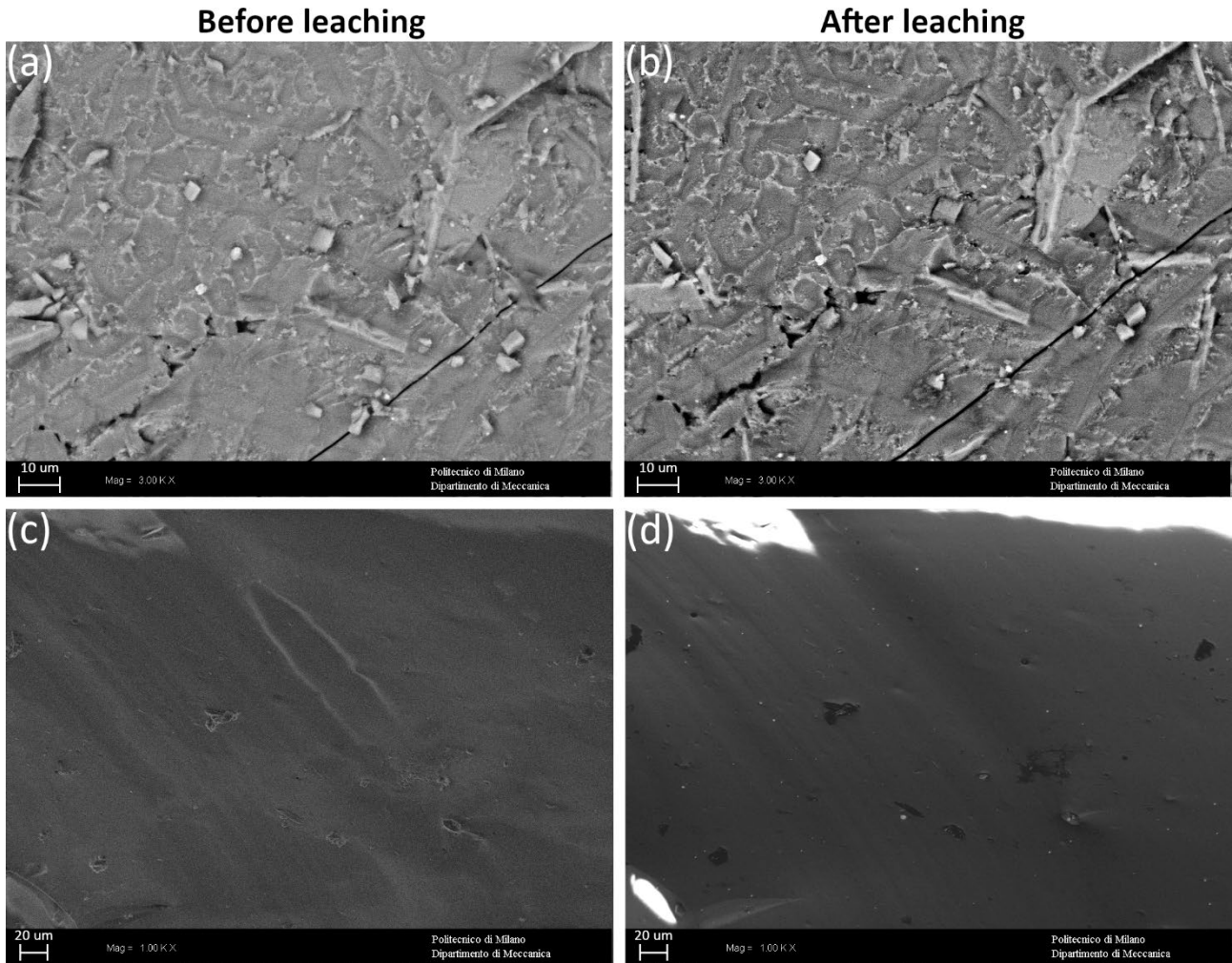
Before leaching   **After leaching**

Figure 7: SEM-BSE pictures before and after leaching test of slag 1 at 10 l/kg (a-b) and slag 2 at 50 l/kg (c-d)

Table 5: SEM-EDS chemical composition of leached slag before and after leaching test (% by weight)

Sample		Na	Al	Si	S	Ca	Ti	Fe
Slag 1	Before leaching	11.48	30.14	25.22	0.84	23.21	9.11	
	After leaching	10.46	30.54	24.61	0.76	22.25	9.80	1.58
Slag 2	Before leaching	10.82	21.77	35.74		24.30	6.20	1.17
	After leaching	9.97	21.57	35.46		24.58	6.86	1.56

3.4. Cast iron characterization

In both the trials, metallic fraction is obtained. With respect the mass charged in the ATP, the metallic fraction accounts for roughly 16 %wt. and this results is in agreement with laboratory tests conducted on the same red muds by the authors [30]. Slight difference in the reduction efficiency was observe between the two tests: with excess of coke (heat 1) the iron recovery was about 95% whereas with stoichiometric amount of coke (heat 2) the iron recovery hardly overcomes the 90%.

The chemical composition of the metallic fractions produced after the reduction of red muds is reported in Table 6. Cast iron 1 has a chemical composition like a hypoeutectic cast iron, very close to the eutectic. Si and Mn are not detected as alloying elements, probably because the conditions in the reduction reactor have not been sufficient to reduce the silicon and to bring it into the metal bath, while Mn is not an element constituting the red mud. P and S are in a lower concentration than that determined in cast iron derived from jarosite sludge [14] and fall within the typical range of unalloyed white cast iron [33]. Cu, Ni, Cr fall within the typical ranges for alloyed gray cast irons, and contribute to increasing mechanical strength and hardness, also acting as anti-graphitizers (promoting the formation of perlite) [33]. Cast iron 2 has

11

practically the same chemical composition of iron 1 but it has a small concentration of Si, probably because the conditions ATP oven were enough to reduce SiO_2 into Si. Except for Cr; Cu, Mo and V are below the typical ranges of alloyed gray cast irons [33].

Table 6. Average chemical composition of cast iron by optical emission spectroscopy (OES) (% by weight).
[1]CE is Carbon Equivalent [42]

Iron	C	CE[1]	Si	P	Cu	S	Cr	Ni	Mo	V	Zn	Nb	Fe
1	3.695	3.851		0.253	0.203	0.175	0.183	0.110	0.048	0.018	0.024		Bal.
2	3.434	3.741	0.384	0.362	0.176	0.142	0.082		0.016	0.045		0.004	Bal.

The microstructure of cast iron 1 appears to be a solidification dendritic, where two distinct structural constituents can be identified: cementite (Fe_3C) and pearlite. Graphite is not observed (Figure 8a). The average length of dendrites is equal to 300-400 μm, whereas dendrite arming spacing (DAS) and secondary dendrite arming spacing (SDAS) are equal to 30 and 5.5 μm respectively, indicating a cooling of approximately 5 °C/s [34,35]. This microstructure is typical of white hypoeutectic fast-cooled cast iron [33,36,37]. The rapid cooling of the metal fraction immediately after the melting has not allowed the carbon to form graphite, leading to the formation of cementite. Rockwell C hardness tests conducted on the sample yield a value of 50 ± 1 HRC, comparable with the literature values for white cast iron, while the Vickers micro-hardness tests conducted on the individual structural constituents unequivocally confirm that the matrix is formed by cementite (890 ± 115 HV0.3/15) and pearlite (338 ± 5 HV0.3/15) [36].

On the contrary, thanks to presence of Si, the cast iron 2 is featured by three different structural constituents: cementite (Fe_3C), pearlite and graphite flakes (Figure 8d). The contemporary presence of graphite and transformed ledeburite is typical of mottled cast iron [33]. The average length of dendrites is equal to 150-250 μm, whereas dendrite arming spacing (DAS) and secondary dendrite arming spacing (SDAS) are equal to 75 and 9 μm respectively, indicating a cooling slightly over 1 °C/s [34,35]. These features are in agreement with the development of graphite, because both Si and low cooling rate promote such a constituent. The Rockwell C hardness tests return an average value of 42 ± 1 HRC whereas the microhardness tests Vickers carried out on the individual structural constituents are 850 ± 55 HV0.3/15 and 375 ± 15 HV0.3/15 for cementite and perlite, respectively [33,36]

On both the irons, two additional non-metallic phases that appear light-coloured in optical microscopy were identified. The analysis in the scanning electron microscopy, coupled with the EDS probe, allowed to measure the chemical composition of the above non-metallic inclusions. They are iron sulphides (average dimension 10-15 μm - orange arrows in Figure 8b and e, Table 7). Around these sulphides and in the interdendritic spaces, steadite (Fe_3P) (an eutectic phase promoted by the high amount of P [38]) can also be identified (green arrows in Figure 8c and f, Table 7).
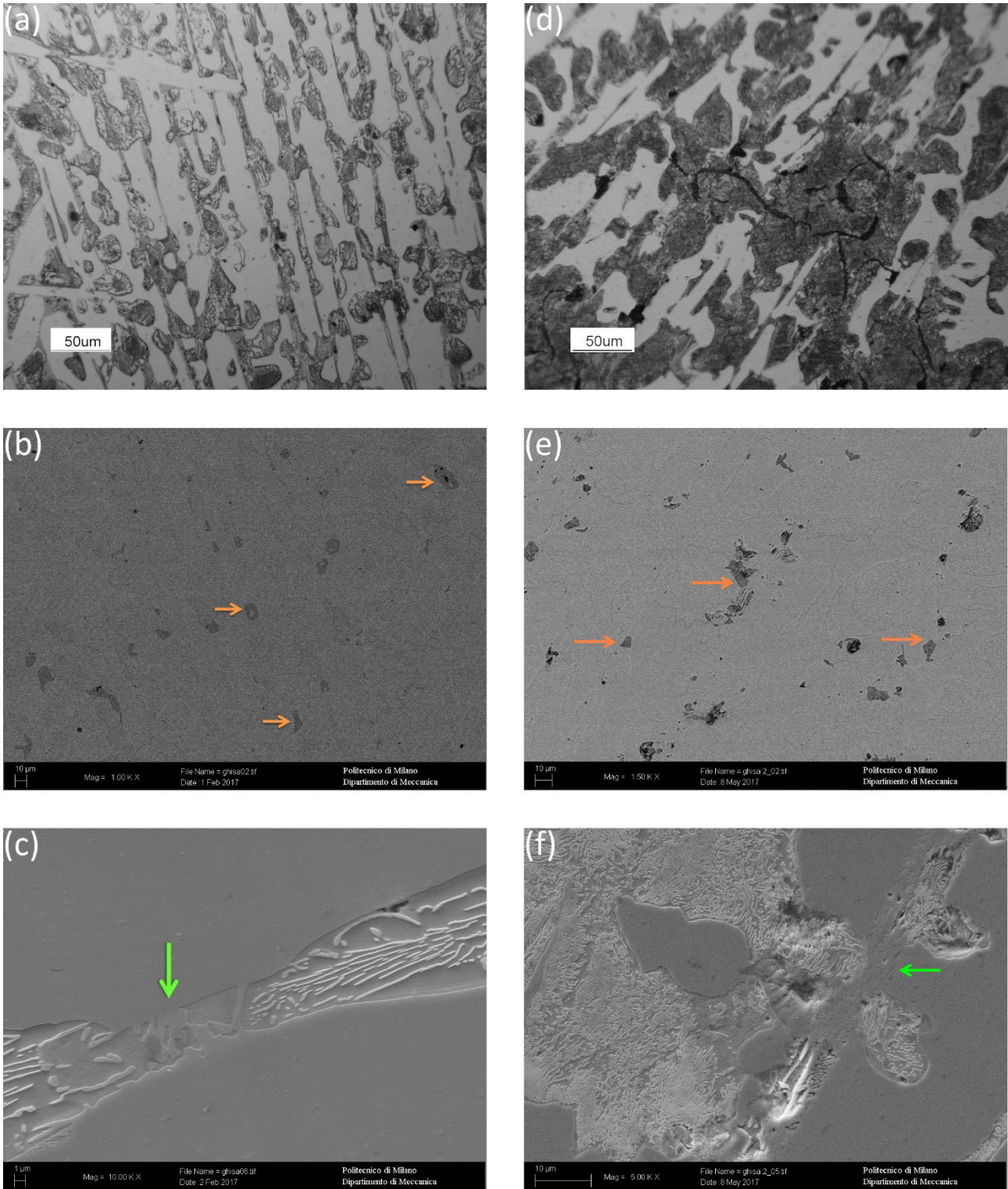
Figure 8. Micrographies of produced cast iron, (a-c) iron 1; (d-f) iron 2. Nital etched 2%. (a,d) OM; (b,e) SEM-BSE; (c,f) SEM-SE

Table 7. SEM-EDS chemical composition range of sulphides and steadite (% by weight)

% in peso	P	S	Fe	As	Cr	Ti
sulphides	0.5-1.0	35.0-38.6	53.06-63.7		0-1.25	0-6.0
steadite	7.6-12.0		85.9-89.7	1.5-2.7		

The moderate concentration of Cu, S, P and S may hinder a direct use of these Fe-base by-product for foundry applications, unless combined with other clean raw materials. These products may be used as an

alternative source of iron in converter (BOF) or electric arc furnace (EAF). However, the presence of Cu could entail casting problems during the steel production line. Therefore, in this case too, use it as a raw material must be combined with other raw Cu-free materials. Nevertheless, it can be used for foundry applications after a refining treatment, to reduce the concentration of harmful elements.

Melting temperature definition is important, since it gives an indication of the energy requested for further treatments.

To identify the transformation temperatures of the produced cast iron, different DSC tests were carried out at 20 °C/min (Figure 9). Transformation temperatures are set out in Table 8.
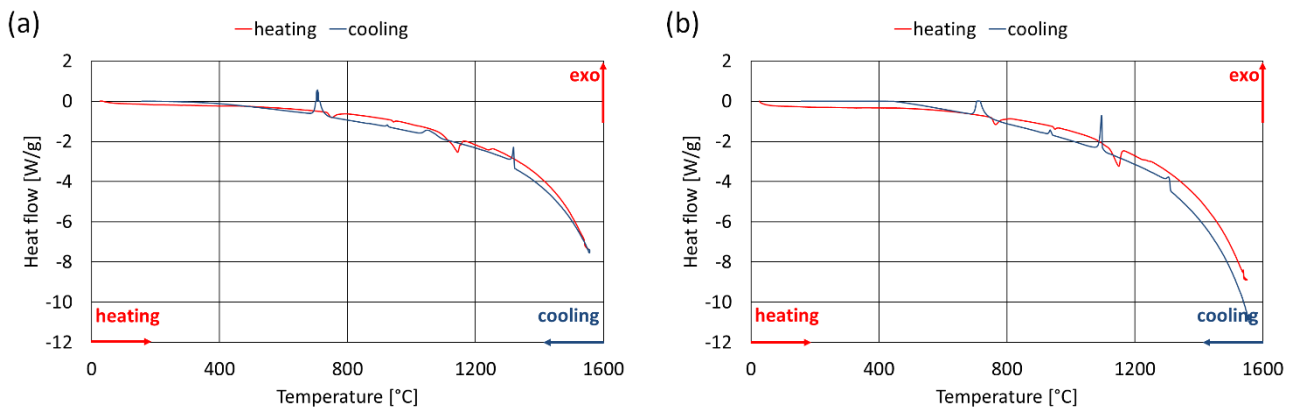

Figure 9. DSC heat flow curves of cast iron at different scanning rates: (a) iron 1, (b) iron 2

Table 8. Transformation temperatures on heating and cooling steps determined by a DSC analysis

Scanning rate 20 °C/min	Iron 1		Iron 2		Transformation
	Onset [°C]	Peak [°C]	Onset [°C]	Peak [°C]	
heating	736	751	751	765	$\alpha+Fe_3C+Fe_3P \rightarrow \gamma+Fe_3C+Fe_3P$
	937	943	943	950	$\gamma+Fe_3C+Fe_3P \rightarrow \gamma+Fe_3C$
	1107	1143	1118	1150	$\gamma+Fe_3C \rightarrow \gamma+L$
	1231	1238	1193	1221	Melting
cooling	1323	1319	1358	1351	$L \rightarrow \gamma+L$
	1100	1050	1105	1096	$\gamma+L \rightarrow \gamma+Fe_3C$
	935	921	943	933	$\gamma+Fe_3C \rightarrow \gamma+Fe_3C+Fe_3P$
	744	704	760	711	$\gamma+Fe_3C+Fe_3P \rightarrow \alpha+Fe_3C+Fe_3P$

The transformation temperatures identified by a differential scanning calorimetry differ from the equilibrium temperature transformations shown on the Fe-C (or Fe-Fe₃C) diagram, because of the effect of the alloying elements on such transformation temperatures [39–42]. In particular, P increases the temperature of the eutectoid transformation, expanding the range in which the sequence of transformations γ-Fe+Fe₃C → γ-Fe+α-Fe+Fe₃C → P+Fe₃C (P: pearlite) can be distinguished. In addition, P has the same effect of Si on the separation between the eutectoidic transformation starting and ending greatly lowers the solidification temperature. Over 0.1% of P steadite (Fe₃P) starts to form [43,44]. Small differences can be highlighted between the two irons, due to the small differences in chemical composition. However, the phase transformations are the same for both the samples. In addition, at 20 °C/min, the precipitation of graphite is hindered whereas for the same alloys at 10 °C/min, some graphite flakes were found. This confirm that the two cast irons have undergone different cooling rate during the production. Thus, it would be possible to control the final microstructure by influencing the cooling rate.

CONCLUSIONS

In this paper, thermal plasma was applied for red muds treatment. Both the slag and the cast iron obtained after red muds reduction were investigated. Based on the results thus obtained, different valuable by-products can be obtained through the proposed technique:

- Exceeding amount of coke and high basicity feeding material (>1) lead to a better reduction with a limited amount of residual iron oxide in the resulting crystalline slag. However, stoichiometric coke ratio and basicity of the feeding material close to 1 lead to the fully vitrification of the slag.
- The slag produced as a result of the reduction of red muds is a quinary compound SiO_2-Al_2O_3-CaO-Na_2O-TiO_2. Both the slags manifest nor morphological neither chemical variation after leaching test; thus, they can be considered inert and safely be disposed of without any further treatment. They could be also recovered as artificial aggregates for civil applications but the compliance with environmental regulation must be verified.
- The product of the red muds reduction is an iron-based alloy. By controlling the cooling, it is possible to control the microstructural features by obtaining white or mottled cast iron. The modest concentration of P, S and Cu may hinder its direct use as steelmaking and foundry raw material, unless combined with clean Cu-free raw materials.

The ATP process can lead to a reset of red muds deposit, avoiding its lagooning, to produce high-value by-products, in line with the "zero waste" philosophy supported by the European Union. Thanks to the promising results obtained at laboratory scale, the industrial transfer of the proposed process was evaluated and the implementation of an industrial scale pilot plant is scheduled within a few years.

REFERENCE

[1]   Standing Committee of the National People's Congress, Environmental Protection Law of the People's Republic of China, China, 2015. http://greenaccess.law.osaka-u.ac.jp/wp-content/uploads/2019/03/Environmental-Protection-Law-of-the-Peoples-Republic-of-China-2014-Revision.pdf.

[2]   European Comission, Directive (EU) 2018/851 of the European Parliament and of the Council of 30 May 2018 amending Directive 2008/98/EC on waste, Off. J. Eur. Union. (2018) 109–140. https://doi.org/10.1023/A:1009932427938.

[3]   Ministero dell'Ambiente, Italian Legislative Decree 152/2006: Environmental standards, Gazzetta Ufficiale Serie Generale n. 88 del 14/04/2006 - Supplemento Ordinario n. 96, Italy, 2006. https://www.gazzettaufficiale.it/atto/serie_generale/caricaDettaglioAtto/originario?atto.dataPubblicazioneGazzetta=2006-04-14&atto.codiceRedazionale=006G0171.

[4]   J. Heberlein, A.B. Murphy, Thermal plasma waste treatment, J. Phys. D. Appl. Phys. 41 (2008) 053001. https://doi.org/10.1088/0022-3727/41/5/053001.

[5]   A.M. Ali, M.A. Abu Hassan, R.R.K. Ibrahim, A.A. Jalil, N.H. Mat Nayan, B.I. Abdulkarim, A.H. Sabeen, Analysis of Solid residue and Flue Gas from Thermal Plasma Treatment of Petroleum Sludge, J. Environ. Chem. Eng. 7 (2019) 103207. https://doi.org/10.1016/j.jece.2019.103207.

[6]   J. Bień, P. Celary, B. Morzyk, J. Sobik-Szołtysek, K. Wystalska, Effect of additives on heavy metal immobilization during vitrification of tannery sewage sludge, Environ. Prot. Eng. 39 (2013) 33–40. https://doi.org/10.5277/EPE130204.

[7]   P. Celary, J. Sobik-Szołtysek, Vitrification as an alternative to landfilling of tannery sewage sludge, Waste Manag. 34 (2014) 2520–2527. https://doi.org/10.1016/j.wasman.2014.08.022.

[8]   A. Mountouris, E. Voutsas, D. Tassios, Plasma gasification of sewage sludge: Process development and energy optimization, Energy Convers. Manag. 49 (2008) 2264–2271. https://doi.org/10.1016/j.enconman.2008.01.025.

[9]   O.L. Li, Y. Guo, J.S. Chang, K. Urashima, N. Saito, A new approach of nonpoint source pollution/stormwater sludge treatment by an integrated thermal plasma system, Int. J. Environ. Sci. Technol. 12 (2015) 1769–1778. https://doi.org/10.1007/s13762-014-0570-7.

[10] C.-T. Li, W.-J. Lee, K.-L. Huang, S.-F. Fu, Y.-C. Lai, Vitrification of Chromium Electroplating Sludge, Environ. Sci. Technol. 41 (2007) 2950–2956. https://doi.org/10.1021/es062803d.

[11] A. Leal Vieira Cubas, M. de Medeiros Machado, M. de Medeiros Machado, F. Gross, R.F. Magnago, E.H.S. Moecke, I. Gonçalvez de Souza, Inertization of Heavy Metals Present in Galvanic Sludge by DC Thermal Plasma, Environ. Sci. Technol. 48 (2014) 2853–2861. https://doi.org/10.1021/es404296x.

[12] E. Sobiecka, L. Szymanski, Thermal plasma vitrification process as an effective technology for fly ash and chromium-rich sewage sludge utilization, J. Chem. Technol. Biotechnol. 89 (2014) 1115–1117. https://doi.org/10.1002/jctb.4221.

[13] I. Mohai, J. Szépvölgyi, Treatment of particulate metallurgical wastes in thermal plasmas, Chem. Eng. Process. Process Intensif. 44 (2005) 225–229. https://doi.org/10.1016/j.cep.2004.04.008.

[14] D. Mombelli, C. Mapelli, C. Di Cecca, S. Barella, A. Gruttadauria, M. Ragona, M. Pisu, A. Viola, Characterization of cast iron and slag produced by jarosite sludges reduction via Arc Transferred Plasma (ATP) reactor, J. Environ. Chem. Eng. 6 (2018) 773–783. https://doi.org/10.1016/j.jece.2018.01.006.

[15] K. Jayasankar, P.K. Ray, A.K. Chaubey, A. Padhi, B.K. Satapathy, P.S. Mukherjee, Production of pig iron from red mud waste fines using thermal plasma technology, Int. J. Miner. Metall. Mater. 19 (2012) 679–684. https://doi.org/10.1007/s12613-012-0613-3.

[16] S.S. Rath, A. Pany, K. Jayasankar, A.K. Mitra, C.S. Kumar, P.S. Mukherjee, B.K. Mishra, Statistical Modeling Studies of Iron Recovery from Red Mud Using Thermal Plasma, Plasma Sci. Technol. 15 (2013) 459–464. https://doi.org/10.1088/1009-0630/15/5/13.

[17] B. Bhoi, P.R. Behera, C.R. Mishra, Production of green steel from red mud: A novel concept, in: T. Jiang, J.-Y. Hwang, G.R.F. Alvera F., O. Yucel, X. Mao, H.Y. Sohn, N. Ma, P.J. Mackey, T.P. Battle (Eds.), TMS Annu. Meet., TMS (The Minerals, Metals & Materials Society), 2015: pp. 19–26.

[18] D. Mombelli, C. Mapelii, C. Di Cecca, S. Barella, A. Gruttadauria, Red mud reduction through blast furnace sludge for cast iron production, Metall. Ital. 108 (2016) 23–41.

[19] A. Imerito, Process and reactor for the plasma transformation of powdery by-products of bauxite processing into a solid, inert and compact product, WO/2012/049696, 2012. http://www.freepatentsonline.com/WO2012049696.html.

[20] D. Mombelli, C. Mapelli, S. Barella, C. Di Cecca, G. Le Saout, E. Garcia-Diaz, The effect of chemical composition on the leaching behaviour of electric arc furnace (EAF) carbon steel slag during a standard leaching test, J. Environ. Chem. Eng. 4 (2016) 1050–1060. https://doi.org/10.1016/j.jece.2015.09.018.

[21] J.A. Duffy, Optical Basicity: A Practical Acid-Base Theory for Oxides and Oxyanions, J. Chem. Educ. 73 (1996) 1138. https://doi.org/10.1021/ed073p1138.

[22] A. Streckeisen, Classification and nomenclature of plutonic rocks, Geol. Rundschau. 63 (1974) 773–786.

[23] A. Streckeisen, IUGS Subcommission on the Systematics of Igneous Rocks: Classification and nomenclature of volcanic rocks, lamprophyres, carbonatites and melilitic rocks; recommendation and suggestions, Neues Jahrb. Für Mineral. Abhandlungen. 134 (1978) 1–14.

[24] M.J.L. Bas, R.W.L. Maitre, A. Streckeisen, B. Zanettin, A chemical classification of volcanic rocks based on the total alkali-silica diagram, J. Petrol. 27 (1986) 745–750. https://doi.org/10.1093/petrology/27.3.745.

[25] H. De La Roche, Classification et nomenclature des roches ignees; un essai de restauration de la convergence entre systematique quantitative, typologie d'usage et modelisation genetique, Bull. La Société Géologique Fr. II (1986) 337–353. https://doi.org/10.2113/gssgfbull.ii.2.337.

[26] H.S. Yoder, C.E. Tilley, Origin of basalt magmas: An experimental study of natural and synthetic rock systems, J. Petrol. 3 (1962) 342–532. https://doi.org/10.1093/petrology/3.3.342.

[27] A. Philpotts, J. Ague, Principles of Igneous and Metamorphic Petrology, Cambridge University Press, 2009. https://doi.org/10.1017/cbo9780511813429.

[28] M.G. Best, Igneous and metamorphic petrology., in: Igneous Metamorph. Petrol., Freeman, 1982.

https://doi.org/10.1029/eo064i023p00404.

[29] W. Cross, J.P. Iddings, L. V. Pirsson, H.S. Washington, Modifications of the "Quantitative System of Classification of Igneous Rocks," J. Geol. 20 (1912) 550–561. https://doi.org/10.1086/621996.

[30] D. Mombelli, S. Barella, A. Gruttadauria, C. Mapelli, Iron recovery from Bauxite Tailings Red Mud by thermal reduction with blast furnace sludge, Appl. Sci. 9 (2019). https://doi.org/10.3390/app9224902.

[31] D. Mombelli, C. Mapelli, S. Barella, A. Gruttadauria, G. Le Saout, E. Garcia-diaz, The efficiency of quartz addition on electric arc furnace (EAF) carbon steel slag stability, J. Hazard. Mater. 279 (2014) 586–596. https://doi.org/10.1016/j.jhazmat.2014.07.045.

[32] Ministero dell'Ambiente, Italian Ministerial Decree: Identification of non-hazardous waste subjected to simplified recovery procedures pursuant to Articles 31 and 33 of Legislative Decree of 5th February 1997, n. 22, Gazzetta Ufficiale Serie Generale n.88 del 16/04/1998, Roma, Italy, 1998.

[33] J.R. Davis, ASM Specialty Handbook Cast Irons, 1996. https://doi.org/10.1016/S0924-6509(08)70274-5.

[34] M.M. Jabbari Behnam, P. Davami, N. Varahram, Effect of cooling rate on microstructure and mechanical properties of gray cast iron, Mater. Sci. Eng. A. 528 (2010) 583–588. https://doi.org/10.1016/j.msea.2010.09.087.

[35] L. Elmquist, A. Diószegi, Relation between SDAS and eutectic cell size in grey iron, Int. J. Cast Met. Res. 23 (2010) 240–245. https://doi.org/10.1179/136404610X12693537269895.

[36] H.T. Angus, Cast Iron: Physical and Engineering Properties, Butterworht & Co, London, 1976. https://doi.org/10.1016/c2013-0-01035-3.

[37] Casting, in: ASM Handb., ASM International, Materials Park (OH), 2008: pp. 41–55.

[38] M. Durand-Charre, Microstructure of steels and cast irons, Springer Science and business media, 2013.

[39] R. Przeliorz, J. Piątkowski, Investigation of phase transformations in ductile cast iron of differential scanning calorimetry, IOP Conf. Ser. Mater. Sci. Eng. 22 (2011) 12–19. https://doi.org/10.1088/1757-899X/22/1/012019.

[40] F. Binczyk, A. Tomaszewska, A. Smoliński, Calorimetric analysis of heating and cooling process of nodular cast iron, Arch. Foundry …. 7 (2007) 25–30. http://www.afe.polsl.pl/index.php/pl/magazine/get/8/calorimetric-analysis-of-heating-and-cooling-process-of-nodular-cast-iron.

[41] M. Pirnat, P. Mrvar, J. Medved, A thermodynamic and kinetic study of the solidification and decarburization of malleable cast iron, Mater. Tehnol. 45 (2011) 529–535.

[42] R. Ivanova, W. Sha, S. Malinov, Differential scanning calorimetry and microscopy study of transformations in ductile cast irons: Part I. Continuous heating, ISIJ Int. 44 (2004) 886–895. https://doi.org/10.2355/isijinternational.44.886.

[43] V. Raghavan, C-Fe-P (Carbon-Iron-Phosphorus), J. Phase Equilibria Diffus. 25 (2004) 541–542. https://doi.org/10.1007/s11669-004-0070-4.

[44] Fe-C-P phase diagram, (n.d.). https://hapli.wordpress.com/forum-ferro/phosphide-eutectic-steadite-pada-besi-cor/ (accessed April 24, 2020).